Irrigation Science (2021) 39:123–143
https://doi.org/10.1007/s00271-020-00708-w

ORIGINAL PAPER

Soil electrical resistivity monitoring as a practical tool for evaluating irrigation systems efficiency at the orchard scale: a case study in a vineyard in Central Chile

J. Araya Vargas[1,2] · P. M. Gil[3] · F. J. Meza[4,5] · G. Yáñez[1,6] · G. Menanno[1,7] · V. García-Gutiérrez[4,8] · A. J. Luque[9] · F. Poblete[3] · R. Figueroa[1,2] · J. Maringue[1] · N. Pérez-Estay[2,7] · J. Sanhueza[1]

Received: 31 January 2020 / Accepted: 21 October 2020 / Published online: 4 November 2020

Abstract
In many orchards, irrigation scheduling is designed based on data from meteorological networks and considering homogeneous soil properties. Such assumptions may result in inefficient irrigation, which is difficult to constrain without expensive or invasive techniques. Here we have evaluated the ability of the electrical resistivity tomography (ERT) for detecting meter-scale irrigation uniformity and deep percolation during irrigation. The spatiotemporal variability of soil volumetric water content (VWC) in a vineyard located near Santiago (Chile) was inferred using ERT monitoring of two irrigation cycles. The electrical resistivity structure up to 4 m depth was estimated using two-dimensional inversion of ERT data. ERT results were verified by comparing resistivity models with VWC measured with soil moisture sensors, soil properties mapped in a 2 m-depth soil pit, and the spatiotemporal evolution of VWC obtained by solving numerically Richards equation. Largest temporal variations of resistivity were observed within the root depth (1 m) and are consistent with expected relative changes in VWC during irrigation. ERT images exhibit lateral changes in resistivity at these depths, likely indicating non-uniform infiltration of water controlled by observed soil texture variations. Resistivity changes were also observed below the root zone, suggesting that a fraction of the irrigation water percolates downward. These findings can be explained by an excess of irrigation water applied during the monitoring, which was planned considering regional evapotranspiration (ET) data that overestimated the actual ET measured at the vineyard. Altogether, our results suggest that ERT monitoring during irrigation is a cost-effective tool to constrain the performance of irrigation systems.

Introduction

For more than a decade, Central Chile is experiencing a severe meteorological drought with important consequences on water availability (e.g. Garreaud et al. 2017, 2019). This drought is consistent with climate change projections. Global Circulation Models results indicate a strong signal of reduction in precipitation for this region that severely challenges water security goals (Meza et al. 2014). Irrigated agriculture in Central Chile is one of the sectors that has the highest rates of fresh water consumption estimated roughly around 70–80% of water

✉ J. Araya Vargas
jaarayav@ing.puc.cl

1 Departamento de Ingeniería Estructural y Geotécnica, Pontificia Universidad Católica de Chile, Santiago, Chile

2 Centro de Excelencia en Geotermia de los Andes (CEGA), Universidad de Chile, Santiago, Chile

3 Departamento de Fruticultura y Enología, Facultad de Agronomía e Ingeniería Forestal, Pontificia Universidad Católica de Chile, Santiago, Chile

4 Departamento de Ecosistemas y Medio Ambiente. Facultad de Agronomía e Ingeniería Forestal, Pontificia Universidad Católica de Chile, Santiago, Chile

5 Centro Interdisciplinario de Cambio Global, Pontificia, Universidad Católica de Chile, Santiago, Chile

6 Núcleo Milenio Trazadores de Metales, Universidad de Chile, Santiago, Chile

7 Dirección Nacional de Fronteras y Límites del Estado (DIFROL), Ministerio de Relaciones Exteriores, Santiago, Chile

8 Departamento de Ingeniería Agrícola, Facultad de Agronomía, Universidad Central de Venezuela, Caracas, Venezuela

9 Departamento de Ingeniería Hidráulica y Ambiental, Pontificia Universidad Católica de Chile, Santiago, Chile

withdrawals (DGA 2012; Valdés-Pineda et al. 2014). In this context, increasing water use efficiency and improving irrigation management is critical for agriculture and to ensure a sustainable development of the region. Although it is usually assumed that drip irrigation systems have a relatively high efficiency (e.g. 90%, see Brower et al. 1989), such efficiency can be significantly lowered by some conditions, such as soil properties, and inadequate irrigation scheduling. Consequently, achieving high levels of irrigation efficiency is of utmost importance considering the global-warming and temporally-extensive droughts recorded since 1950 worldwide (Dai 2013).

Correct measurement of irrigation efficiency (defined here as the amount of water retained by soils after an irrigation event over the amount of water applied; Israelsen 1950) is critical because crop productivity is highly dependent on water transpiration. A deficiency on soil water availability may result in crop water stress and experience yield reduction; on the contrary, an excess of soil water availability reduces oxygen diffusion to roots and creates root hypoxia with detrimental results. In addition, the excess of water applied usually percolates and moves nutrient away from the root zone contaminating water bodies and reducing nutrient uptake. Traditional methods to measure or monitor irrigation efficiency are mostly based in direct soil water content measurements and soil moisture estimations. The only direct water content measurement (the gravimetric method; Reynolds 1970) is slow, impossible to obtain in real time scale and requires intensive sampling to obtain a realistic representation of spatial variability. Methods commonly used to estimate soil moisture at orchard scale are based in dielectric constant measurements of the soil and employ technologies based on Time Domain Reflectometry (TDR) or Frequency Domain Reflectometry (FDR) (Evett and Parkin 2005; Robinson et al. 2008). These methods perform relatively well in mineral soils, are friendly to be used at orchard scale, and allow users to make quick decisions regarding irrigation management. However, dielectric constant measurements are point based and cannot capture the spatial heterogeneity of the system or do require a set of measurements and equipment that increases operational cost and adds complexity to irrigation scheduling and management. Also, these systems use probes with only 15–20 cm as radium of influence, which implies the need to install many sensors in order to obtain a depth moisture profile, and several monitoring stations in the orchards, to have a representative measurement of soil moisture in the field. Even in pressurized systems, soil heterogeneity may cause big differences in terms of water movement or water retention capacity reducing their efficiency of application. The lack of resources and time lead managers to base irrigation decisions on point measurements and general soil studies with suboptimal results. This problem motivates having a quantitative knowledge of the spatial distribution of soil moisture, which could be solved with technologies such as geophysical methods.

Geophysical methods have the ability to map comparatively larger volumes of soil with the advantage of minor perturbation of the soil structure (e.g. Allred et al. 2008). The electrical resistivity tomography (ERT) is one of the most common geophysical techniques used in agricultural applications (e.g. Samouëlian et al. 2005). The ERT method estimates the distribution of electrical resistivity in the subsurface from measurements of electrical potentials which result from injection of electrical currents to the soil. Although the bulk electrical resistivity of a soil volume depends on a myriad of factors, it is usually strongly dependent on the electrical resistivity and amount of interstitial fluids (e.g. Friedman 2005). For the latter reason, ERT has been widely employed to characterize the soil water content in a variety of agricultural contexts, from the field scale (e.g. Brunet et al. 2010; Calamita et al. 2012; Moreno et al. 2015; Alamry et al. 2017) to the scale of plant roots (e.g. Garré et al. 2011; Cassiani et al. 2015). The ground penetrating radar (GPR) has been used to image soil structure and to estimate soil water content (Huisman et al. 2003; Klotzsche et al. 2018). GPR is a geophysical method that uses high-frequency electromagnetic (EM) waves that are transmitted and reflected within the subsurface. Since the propagation of EM waves depends on the electrical permittivity and electrical resistivity of the subsurface, information such as the travel time of the EM ground wave or the amplitude of the reflected waves can be used to estimate the water content (e.g. Hubbard et al. 2002; Huisman et al. 2003) and salinity in soils (Hagrey and Müller 2000).

A number of studies have used ERT to monitor soil hydraulic dynamics during irrigation, usually in combination with other geophysical techniques (e.g. GPR) and using micrometeorological constraints (e.g. evapotranspiration fluxes measured with eddy covariance sensors). At the plant scale, ERT monitoring have obtained high-resolution images revealing complex patterns in the soil hydraulic dynamics around plant roots (e.g. Cassiani et al. 2016; Mary et al. 2018, 2019). Such knowledge has provided insights into the efficiency of irrigation fronts to satisfy plant needs (e.g. Cassiani et al. 2015). Yet, it is still poorly understood how the characterization of soil parameters at a single plant can be upscaled in order to make irrigation decisions for a plot or orchard. Although some authors have reported that mapping meter-scale variability of soil electrical resistivity provides a useful proxy for changes in soil moisture and composition at the orchard scale (e.g. Michot et al. 2003; André et al. 2012; Vanella et al. 2018), there are studies showing that temporal changes in electrical resistivity cannot be unambiguously related to soil moisture variability (e.g. Moreno et al. 2015; Hardie et al. 2018). The validity of electrical resistivity as a proxy for soil moisture is strongly sensitive to local soil conditions (e.g. Brillante et al. 2014). Electrical

resistivity is a good proxy for soil moisture variability only if there is a significant contrast between the resistivity of interstitial fluids and the resistivity of matrix components. Otherwise, misleading estimates of soil moisture can be derived from resistivity images in soils where fluids and matrix have similar resistivity (see e.g. Waxman and Smits 1968), or where fluids with significantly different resistivities are mixed (Boaga et al. 2013; Moreno et al. 2015; Cassiani et al. 2016; Hardie et al. 2018). To establish a relationship between electrical resistivity and soil moisture, ERT results are usually calibrated with measurements using soil moisture sensors such as TDR (see e.g. Calamita et al. 2012). Most of ERT studies monitoring irrigation dynamics have been focused in characterizing the distribution of soil moisture from the surface until the root zone depth, revealing that irrigation water can follow complex paths during infiltration, resulting sometimes in low degree of irrigation uniformity (e.g. Moreno et al. 2015; Hardie et al. 2018). However, the applicability of ERT to detect infiltration of irrigation water below the root zone (i.e. deep percolation) has not been completely addressed.

In this study, we aimed to determine whether ERT provides useful and practical insights to constrain meter-scale irrigation uniformity and deep percolation, two parameters that are important for assessing the efficiency of irrigation systems at the orchard scale. Our hypothesis was that meter-scale temporal variations in the electrical resistivity structure are sensitive enough to detect relative changes in soil moisture triggered by infiltration of irrigation water. To test our hypothesis, we monitored with time-lapse ERT the spatiotemporal distribution of soil moisture along a vine row at different stages of the irrigation cycle. To characterize shallow irrigation uniformity and deep percolation at the orchard scale demands a compromise between resolution and depth of exploration of ERT surveys which is not trivial to address with timely-efficient measurements. To tackle this issue, we measured ERT data using two modes of acquisition. ERT results were verified by comparing electrical resistivity models with GPR data, soil properties mapped in a soil pit dug next to the studied vine row, soil moisture measured with TDR and FDR sensors, and a numerical model of the soil hydraulic dynamics constrained by time series of evapotranspiration (ET) and soil moisture data. Based on this analysis, we evaluate the efficacy and limitations of ERT to characterize meter-scale soil moisture heterogeneity, and discuss some potential practical applications of ERT monitoring results for making irrigation decisions.

Materials and methods

Study site

The study was conducted in a Cabernet Sauvignon (*Vitis vinifera*) vineyard (33.7048° S, 70.5758° W, 706 m average altitude) located in the area of Pirque, distant 30 km south of the city of Santiago de Chile (Fig. 1a, b). This region is characterized by a Mediterranean climate, with precipitation concentrated mostly in winter (i.e. from June to August with annual total precipitation in the order of 300 mm; Marchant et al. 2007). Mean annual temperature is about 14.5 °C with 60% relative humidity. In the studied vineyard, the vine rows are North–South oriented in a vertically trilled system with 1.94 m height. The space between rows is 2.45 m, while vines are planted at 1.20 m spacing. The vineyard was irrigated using a drip system with lines along the vine rows, a spacing of 0.6 m between drip emitters and a total discharge of 4 L per hour. During the study, irrigation events took place every 6 days for an interval of 10 h and using a flow rate of 2.7 mm per hour. The amount of water applied in the irrigation events was planned based on reference evapotranspiration, which is estimated from data collected by a nearby weather station. Using this information, the applied water is decided to supply a fraction of cumulative reference evapotranspiration which is slightly above the crop coefficient ($K_c = 0.65$).

Geophysical experiments were focused on a segment of a vine row which was permanently monitored by a TDR and an eddy covariance system (Fig. 1c). The volumetric water content (VWC) in one of the adjacent vine rows was measured using a Campbell Scientific Inc CS616 TDR sensor. This TDR was installed vertically at 0.1 m depth below a dripper. Measurements of the VWC were taken every 30 min by TDR. An eddy covariance system was mounted in a tower located approximately 10 m from the studied vine row (see description in "Eddy covariance"). Soil temperature was measured by Campbell Scientific Inc TCAV thermocouples installed at 0.02 m and 0.04 m depth, obtaining an average value every 30 min. A soil pit was dug in the inter row next to the studied vine row on 4 September 2019, approximately one and a half months after the last rain and 4 months after the irrigation season. The soil pit extended parallel to the ERT profile from $X = 3.3$ m to $X = 12.8$ m (Fig. 2), and reached a maximum depth of 1.8 m. The soil profile was described in four columns inside the soil pit at $X = 4$, 5, 7 and 9 m (see Table 1 and Fig. 2a). At each column, we characterized the soil texture, roots density and bulk apparent density. In addition, we measure VWC along each column with 30 cm sample interval using a FDR Decagon GS1 Volumetric Water Content sensor (see Table 1). Both TDR and FDR instruments were calibrated using the calibration curves provided by the manufacturer for loamy soils. A total of 0.5–1 kg of disturbed soil samples were taken from each representative soil horizon for obtaining bulk apparent density and soil granulometry. Bulk apparent density was measured using the clod method (Cunningham and Matelski 1968). Soil granulometry was obtained by using the hydrometer method (Bouyoucos 1962). From granulometry results, we

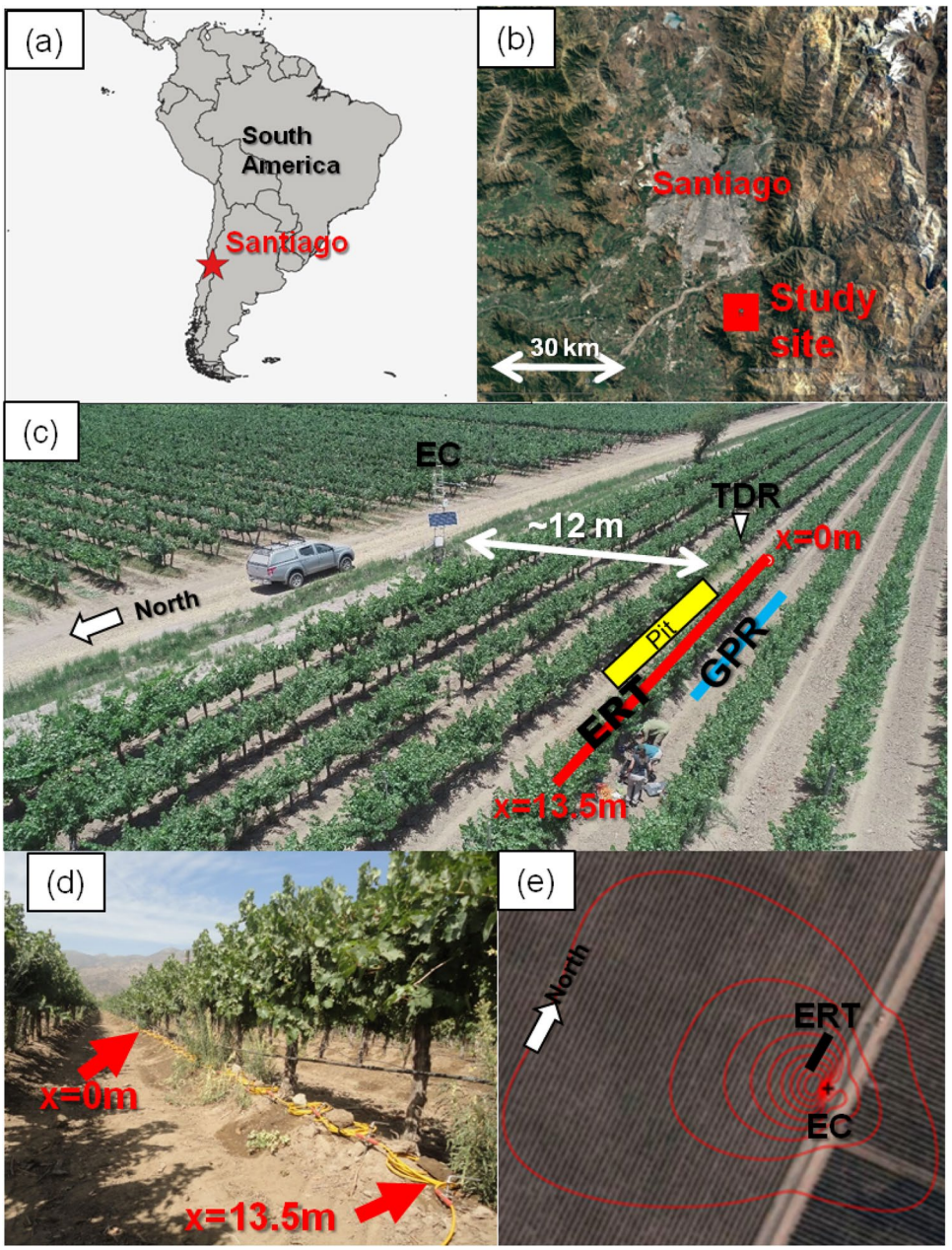

Fig. 1 **a**, **b** Location of the study area. **c** Experiment layout. Red and blue lines show the location of the ERT and GPR profiles, respectively. The yellow rectangle indicates the location of the soil pit. *TDR* permanent TDR sensor, *EC* eddy covariance tower. Photo courtesy of Francisco Suárez. **d** Photo depicting the ERT profile (yellow cable below the grapevines) along the vine row. The GPR profile was measure along the interrow behind the grapevines. **e** Map showing the average evapotranspiration footprint interpreted from 8th to 18th January 2019. Contours lines are shown with 10% interval, from 10 to 90% source area

classified the soils using the USDA textural classes (USDA 1977). Soil samples are predominantly loams, sandy loams and loamy sands. It was not possible to obtain undisturbed soil core samples to measure gravimetric water content and hydraulic conductivity. Root size was classified into thick (> 2 mm diameter) and thin (< 2 mm diameter) using the criterion employed by Morlat and Jacquet (1993).

ERT

ERT surveys were carried out along a 13.5 m-long profile during six alternate days of January 2019 (see Table 2), in the middle of the period in which the vineyard was under irrigation (summertime). An additional ERT survey was made on September 23 (early springtime) of the same year to compare ERT results with soil pit observations made in September 4. However, irrigation started during ERT acquisition on September 23, and therefore soil moisture conditions at shallow levels (0–0.5 m depth) were not fully comparable with those observed in the soil pit. All ERT measurements were made using a TIGRE Resistivity Imaging System and 32 stainless-steel electrodes. Electrodes had a length of 40 cm and a diameter of 2 cm, and were buried 15 cm into the soil. Electrodes position and depth did not change during the whole sequence of measurements of January 2019. A dipole–dipole array was employed, using

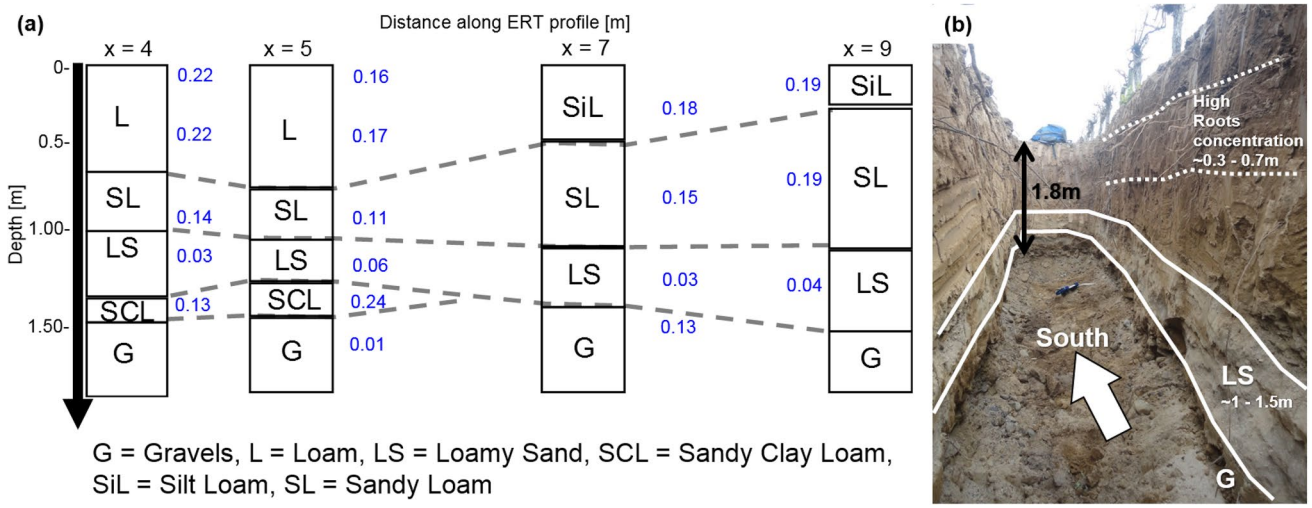

Fig. 2 Soil pit. **a** Soil pit scheme summarizing measured parameters along the four vertical columns studied: blue numbers are average total water content obtained by FDR measurements, labels indicate soil texture according to USDA classification obtained from the granulometric analysis of samples. Gray dotted lines indicate the interpolation of soil horizons between columns. **b** Photo (looking to the south) showing the soil pit. Brownish soil horizons correspond to loam (L), sandy loam (SL) and silt loam (SiL) units. Gray soil horizon constrained by white lines is the loamy sand (LS) unit which includes a lens of sandy clay loam (SCL). The lowest soil horizon is the unit of gravels (G). White dotted lines outline the depths where roots are concentrated

Table 1 Soil characteristics at the soil pit

ERT profile position X (cm)	Depth range (cm)	Bulk density (g/cm^3)	Thick roots (> 2 mm diameter) density (roots per cm^2)	Thin roots (< 2 mm diameter) density (roots per cm^2)	VWC (m^3/m^3)	Clay (%)	Silt (%)	Sand (%)	Soil texture
400	0–20	1.43	0.0023	0.0037	0.2	18	40	42	Loam
400	20–65	1.38	0.00175	0.003	0.22	18	34	48	Loam
400	65–100	1.48	0.001	0.004	0.14	10	36	54	Sandy loam
400	100–120	–	0.0005	0.004	–	–	–	–	Gravels
400	120–140	1.44	0	0	0.03	4	16	80	Loamy sand
400	140–155	–	0	0	0.13	–	–	–	Gravels with clay lenses
400	155–180	–	0	0	–	–	–	–	Gravels
500	0–40	1.41	0.0025	0.0001	0.16	18	36	46	Loam
500	40–75	1.41	0.002	0.003	0.17	16	32	52	Loam
500	75–106	1.43	0	0	0.11	8	24	68	Sandy loam
500	106–130	1.44	0	0	0.06	4	10	86	Loamy sand
500	130–150	–	0	0	0.24	–	–	–	Sandy clay
500	150–180	–	0	0	0.01	–	–	–	Gravels
700	0–47	1.43	0.0016	0.001	0.18	4	56	40	Silt loam
700	47–110	1.37	0.0022	0.001	0.15	4	26	70	Sandy loam
700	110–145	1.34	0.00075	0.00025	0.03	4	8	88	Loamy sand
700	145–180	–	0	0	0.13	–	–	–	Coarse sand
900	0–25	1.48	0.00125	0.00125	0.19	4	50	46	Silt loam
900	25–110	1.4	0.000857	0.00142	0.19	4	30	66	Sandy loam
900	110–160	1.4	0	0	0.04	4	8	88	Loamy sand
900	160–175	–	0	0	0.06	–	–	–	Gravels
900	175–190	–	0	0	0.01	–	–	–	Gravels

Table 2 Dates of geophysical surveys, soil pit characterization and irrigation events

Date	Average soil temperature during survey (°C)	
January 3		Irrigation
January 8, 12:00–13:00	23.0	ERT (5 days after irrigation, only using $N=4$)
January 9		Irrigation
January 10, 13:37–15:35	20.2	ERT (1 day after irrigation)
January 11, 10:44–12:30	19.9	ERT (2 days after irrigation)
January 14, 09:59–11:35	19.1	ERT (5 days after irrigation)
January 15		Irrigation
January 16, 10:53–12:20	21.5	ERT (1 day after irrigation)
January 18, 10:03–11:37	19.4	ERT (3 days after irrigation)
September 4		Soil pit characterization (4 months after irrigation season and 1.5 month after last precipitation)
September 23, 13:00–14:50		ERT and GPR surveys (irrigation started during measurements)

All dates correspond to year 2019

an electrode spacing of 0.5 m. Each point of measurement is defined by a pair of current and potential dipoles, which is called a quadripole as a whole. For each quadripole, the TIGRE system calculates a resistance value and its associated root mean square (RMS) error by stacking three to four measurements.

Two ERT acquisitions were carried out every day over the entire profile using N factors of $N=1$ and $N=4$ (except on January 8 when only $N=4$ was used). The N factor describes the distance between current and potential dipoles which are selected for measuring each quadripole. While the distance between current and potential dipoles for $N=1$ is equal to the electrode spacing (i.e. 1×0.5 m $=0.5$ m), for $N=4$ current and potential dipoles are separated by 4 times the electrode spacing (i.e. 4×0.5 m $=2$ m). The purpose of using these different acquisition modes was to resolve two different targets. Measurements with $N=1$ aimed to obtain a high-resolution image of the electrical resistivity structure until a depth of 1 m, to characterize how uniformly distributed was the soil moisture after irrigation. Measurements with $N=4$ yield a coarser resistivity image but a deeper depth of investigation (until a depth of 3–4 m), to detect resistivity changes potentially related to deep percolation.

The ERT survey was conducted to detect temporal changes in the electrical resistivity of the subsurface. However, variability between ERT results obtained at different days may arise, at least in part, from measuring conditions. To minimize the influence of random and measuring errors, quadripole measurements were discarded from the analysis if at any day: (1) they were associated with observations (electrical resistance value) that exhibit instrumental errors $>2\%$, or (2) they were related to clear artifacts observed in resistivity pseudosections (i.e. outlier points compared to the neighbor resistivity field). Using these criteria, the analyzed dataset for each day comprises 66 quadripoles selected out of 159 for $N=1$, and 158 out of 266 for $N=4$. For measurements with $N=1$, most of the discarded quadripoles are located between horizontal distances of $X=10$ and $X=15$ m. Therefore, the following analysis on the temporal variation of the resistivity structure will be focused between $X=0$ and $X=10$ m, which represents the segment of the ERT section with more reliable data over time and space.

The data were inverted using the Zondres2D software (http://zond-geo.com/english/). To obtain a model of the electrical resistivity structure that explains the observed data (i.e. the resistance calculated from measured current and potential at each quadripole), Zondres2D can solve the inversion problem using different methods. We chose the Occam algorithm (Constable et al. 1987), which uses the least-square method to minimize an objective function that depends on: (1) the misfit between observations and the model response, and (2) a regularization term that privileges smooth models and stabilizes the mathematical solution (Zond geophysical software 2016). To calculate model responses, Zondres2D uses the finite-element method to solve numerically the Poisson equation which relates electrical potential and currents with the resistivity of a medium. The regularization term depends on a smoothing factor parameter, which controls the desired smoothness of the model. After performing inversion tests for each day using smoothing factors of 0.005, 0.3 and 1, we concluded that a smoothing factor of 0.3 resulted in smooth models that fit satisfactorily the data. The inversion tests converged after 2 or 3 iterations (see Tables 4 and 5 in the "Appendix A").

The model space comprised an array of rectangular cells with 0.25 m wide that is half of the electrodes spacing. The thickness of the cells at the top of the model was 0.03 m. Then, the thickness of cells increases with depth with an

incremental factor of 1.1, to account for the decrease in resolution with depth which is inherent to the ERT technique. Data from each day were inverted independently using the parameters described before. In all inversions we used as starting model a homogenous half space of 70 Ωm. The overall fit between observations and model response is good for all the obtained preferred resistivity models (see data misfit obtained for all models in Tables 4 and 5). Models' responses reproduce most patterns observed in apparent resistivity pseudosections (compare observed and calculated pseudosections shown in Figs. 10 and 11).

The electrical resistivity of materials depends on temperature, and therefore we corrected the effect of temperature by calculating the electrical resistivity at 25 °C of all models using the equation of Keller and Frischknecht (1966). Resistivities of each ERT acquisition were corrected considering the average soil temperature recorded by the thermocouple at the same time and date. We applied this correction only to cells of the model located from 0 to 0.4 m depth, because the daily variation of temperature does not significantly affect the subsurface below 0.3 m depth (see e.g. Lowrie 2007). Electrical resistivity values, however, do not change significantly after applying the temperature correction. During ERT measurements temperature fluctuated between 19.1 and 23 °C, resulting in corrected resistivity values that vary from 0.86 to 0.95 of their corresponding uncorrected resistivities.

GPR

GPR measurements were carried out on September 23, 2019, along the two interrows adjacent to the studied vine row. All GPR measurements were made using a MALÅ Easy Locator Pro Wide Range HDR, with a dual wide bandwidth antenna with central nominal frequencies of 160 and 670 MHz. For this work, we only used the high-frequency set of data to map the soil up to 1.8 m below the surface. The low frequency data proved not to be useful, as the pulse emitted by the low frequency antenna does not have the resolution to image the soil immediately below surface nor it was able to penetrate below 2 m. The device has fixed antenna separation, i.e. does not allow multi-offset data acquisition that is better suited for GPR techniques for estimating water content such as ground wave analysis (Huisman et al. 2003) and normal-moveout velocity analysis (Greaves et al. 1996).

GPR data were processed using the software REFLEXW (Sandmeier 2019). We applied a standard processing sequence consisting into the application of an exponential gain function to compensate for the attenuation of the reflected signal, band-pass filter, background removal to remove typical horizontal noise from GPR data, and Kirchhoff migration. We used a constant average velocity of 0.12 m/ns to migrate and convert the two-way-traveltime axis into depth. This velocity was estimated by fitting the strong diffraction hyperbolas visible in the 0.2–1 m depth range.

Eddy covariance

Eddy covariance (EC) carbon and water flux measurements were made by an IRGASON Campbell Scientific Inc that was installed in a tower 4 m above the soil surface. This system comprises a sonic anemometer and an open-path infrared gas analyzer. Measured energy fluxes were recorded with 10 Hz sample frequency by a CR3000 Campbell Scientific Inc datalogger. We analyzed 30-min average net fluxes time series collected from 8 to 18 January. Eddy fluxes were corrected for density perturbations (Webb et al. 1980) and coordinate rotation (Kowalski et al. 1997), and quality–controlled following Reverter et al. (2010). Data quality was assessed looking at Energy Balance Closure based on 30 min average, which had a linear regression slope of 0.82, intercept of 12.7 (W/m^2) and coefficient of regression (R^2) of 0.97 for the period under study. These data represent the ET flux over an area of influence called the footprint. The footprint depends on wind characteristics and some meteorological parameters (Kljun et al. 2004), and therefore it varies dynamically over hours and days. We estimate the footprint in a daily basis and for the entire interval of measurements using the Flux Footprint Prediction (FFP) model (Kljun et al. 2015). The studied vine row is contained in the area of the EC footprint estimated for all ERT acquisition days. This is illustrated in Fig. 1e, which shows the average footprint estimated from 8 to 18 of January.

Numerical model of spatiotemporal distribution of soil moisture

We solved numerically a simplified version of the Richards equation (Richards, 1931) in one dimension. This equation describes the variation of VWC (θ) with depth and time as function of hydraulic diffusivity of the soil (D), its hydraulic conductivity (K) and the amount of moisture that leaves the soil (a sink function S):

$$\frac{\partial \theta}{\partial t} = \frac{\partial}{\partial z}\left(D\frac{\partial \theta}{\partial z} + K\right) - S \quad (1)$$

We solved numerically Eq. (1) using the software FlexPDE©. The model space comprises a medium of 5 m depth (Fig. 3a). Table 3 shows the values of the hydraulic parameters K and D that we used in our numerical models. These parameters vary with depth according to the major soil units characterized in the soil pit. We modeled two scenarios simulating the soil columns observed at $X=4$ m and $X=9$ m in the soil pit (models A and B in Fig. 3b). For each soil unit, we used the hydraulic conductivity values reported in Schaap

(2002). The hydraulic diffusivity D of a soil depends on θ and on its hydraulic conductivity. For each soil, we estimated a constant value of D (Table 3) using the analytical function of Van Genuchten (1980) that relates D and θ. To obtain a constant value of D for each soil, we evaluated the Van Genuchten (1980) function assuming $\theta = 0.39$, which represents a high value that allows stability of the numerical simulation tests. To simulate the hydraulic properties of the gravels observed at the bottom of the soil pit, we modeled this unit as sand.

The sink function S (see Eq. 1) was parameterized as the amount of water loss per time due to ET (see Fig. 3a). As a proxy of ET values, we used the ET flux measured by the EC tower, which yields the volume of water (m^3) per square meter per time released to the atmosphere by ET. In order to obtain the volumetric water content (m^3/m^3) which leaves the soil due to ET in a time unit, we multiplied the ET flux by the vine row surface (m^2), and then divided by the volume of the soil which is occupied by roots. We estimated the total volume of roots as:

$$\text{Total volume of roots} = N_{\text{roots}} \cdot V_{\text{root}} = 0.001885\,[\text{m}^3]$$

where N_{roots} is the number of roots present below a square meter, and V_{root} is the average volume of a single root. N_{roots} was estimated as the average root density over all columns mapped in the soil pit (0.015 [roots/cm^2]) multiplied by the area of the vine row depth section (100×100 [cm^2]). V_{root} was estimated by assuming that each root can be modeled as a cylinder with a radius of 0.2 (cm) and a length of 100 (cm), equivalent to the width of the studied volume. These assumptions yield $V_{\text{root}} = \pi \cdot (0.2)^2 \cdot 100 = 12.56$ (cm^3) and a total root volume of 1.885 (lt) or 0.001885 (m^3). Following the aforementioned procedure, we obtained an estimate of soil moisture lost by ET (grey dots in Fig. 3c). The ET moisture shows a complex shape (see gray dots in Fig. 3c), in which we identify two patterns: a long-term and low-amplitude decaying trend likely related to the decreasing of

Table 3 Hydraulic parameters used in the numerical solution of Eq. (1)

Soil unit	K (m/s)	D (m^2/s)
Loam (L)	1.25×10^{-7}	0.0417
Loamy sand (LS)	2.34×10^{-7}	0.0795
Sand (S)	3.25×10^{-7}	2.5488
Sandy Clay Loam (SCL)	3.25×10^{-7}	0.0201
Sandy Loam (SL)	1.83×10^{-7}	0.0361
Silty loam (SiL)	1.46×10^{-7}	0.0316

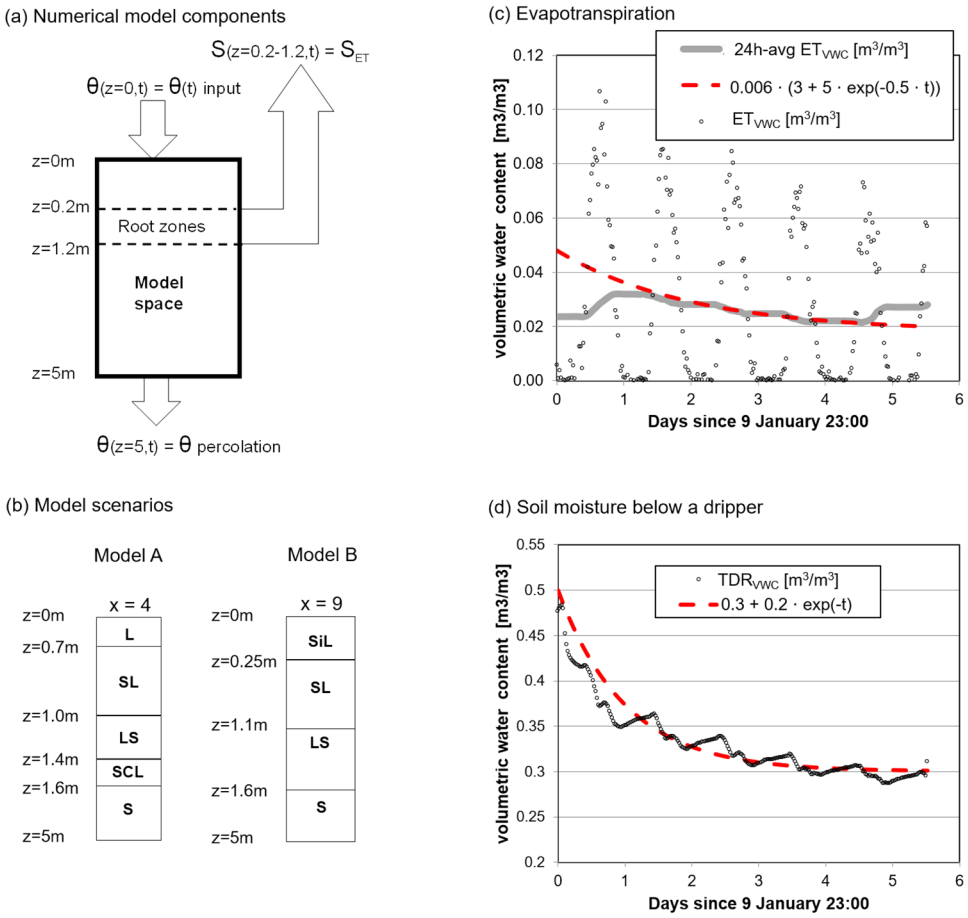

Fig. 3 Parameters of the numerical model of soil moisture. **a** Schematic visualization of the numerical model and its components. **b** Distribution of soil units used in the two modeled scenarios. Hydraulic parameters for each unit are shown in Table 3. *L* loam, *LS* loamy sand, *S* sand, *SCL* sandy clay loam, *SiL* silty loam, *SL* sandy loam. **c**, **d** proxies used for amount of water loss due to evapotranspiration (ET) and irrigation water input, respectively. **c** Gray dots are ET values measured by eddy covariance system expressed as soil moisture (see "Numerical model of spatiotemporal distribution of soil moisture"). The gray line is the 24 h moving average of the ET data, which we interpret as the long-term trend of ET. The red-dashed line is a model that fits the gray line (Eq. 2). **d** Gray dots are soil moisture recorded by TDR sensor installed at 0.1 m depth below a dripper in the adjacent vine row. The red-dashed line is a model of the long-term trend observed in the data (Eq. 3)

soil moisture with time since irrigation, and high-amplitude daily variations likely related to plants' photosynthesis cycle. Daily variations were not considered in our model because the frequency of ERT measurements (one measurement per day) cannot account for such fluctuations. Therefore, we modeled the sink function S using a mathematical expression (Eq. 2 and red-dashed line in Fig. 3c) that fits the long-term pattern of ET measurements (gray line in Fig. 3c).

$$S_{ET} = 0.006 \cdot (3 + 5 \cdot \exp(-0.5 \cdot t)) \quad (2)$$

We assumed that $S = S_{ET}$ (Eq. 2), and set that S extracts water from 0.2 to 1.2 m depth, which is the depth with the maximum concentration of thin roots (Fig. 4, right panel). Our model has two boundary conditions: the amount of input water that is irrigated (θ_{input} in Fig. 3a) and the water percolated below roots ($\theta_{percolation}$ in Fig. 3a). As proxy for the irrigation water input, we use the variation of soil moisture over time measured by the fixed TDR sensor installed below a dripper since the irrigation event on January 9 (Fig. 3d). The soil moisture variation measured by the TDR shows also a complex shape (see gray dots in Fig. 3d), in which we identify again a long-term decaying trend and a daily variation pattern. We modeled the water input using a mathematical function (Eq. 3, red-dashed line in Fig. 3d) which estimates only the long-term drying trend of TDR measurements. Daily variations were not considered because the frequency of ERT measurements cannot account for such fluctuations.

$$\theta_{input} = 0.3 + 0.2 \cdot \exp(-t) \quad (3)$$

A constant moisture of $\theta_{percolation} = 0.15$ was employed as the lower boundary condition, which roughly coincides with the average value of VWC measured in situ in the soil pit. Such measurements were done in springtime, approximately 3 months after irrigation and 1.5 months after the last rain. We assumed, therefore, that $\theta = 0.15$ represents the background VWC, when neither irrigation water nor root water uptake is disturbing the soil water content.

Results

Soil structure

To characterize the soil structure and for calibrating geophysical results, we compared ERT and GPR conducted on 23 September 2019 with soil characterization obtained in the

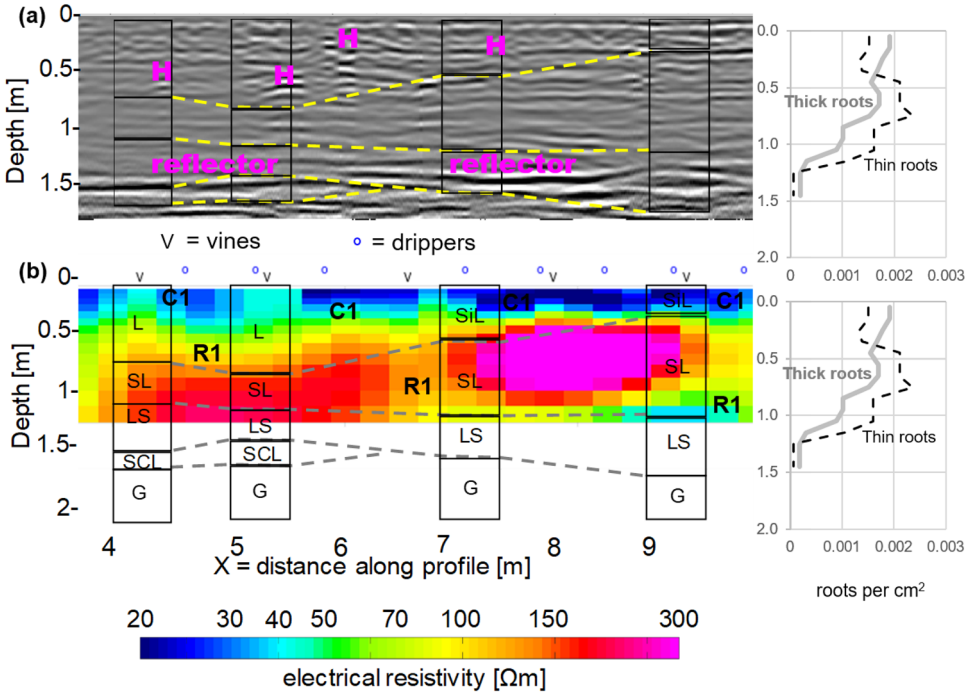

Fig. 4 Comparison between ERT, GPR and soil pit results. The horizons interpreted in the soil pit overly the geophysical sections. Graphs to the right of sections show variation of average density of roots with depth mapped from the four columns at the soil pit. **a** GPR (September 23rd) migrated section measured with a 670 MHz antenna (nominal central frequency). Pink labels indicate major features described in "Soil structure". **b** Extract of electrical resistivity section derived from ERT acquired with $N = 1$ on September 23rd. "V" and "O" on top of the electrical resistivity section indicate position of grapevines and drippers, respectively. *L* loam, *LS* loamy sand, *S* sand, *SCL* sandy clay loam, *SiL* silty loam, *SL* sandy loam. C1 indicates the layer from 0 to 0.5 m depth, which exhibits resistivities < 50 Ωm over all days. R1 refer to bodies with resistivity > 100 Ωm which are observed mostly from 0.5 to 1 m depth

soil pit (see Fig. 4). In September 2019 (i.e. 8 months after the ERT monitoring experiment), soil moisture content was not disturbed neither by irrigation water, rain or root water uptake at least for 2 months, except from 0 to 0.5 m of the geophysical sections that seem to be affected by the irrigation event that started that day. The clearest pattern observed in GPR section is a semi continuous reflector at an approximate depth of 1.5 m (see Fig. 4a), which roughly coincides with the top of the gravels (the brownish strata below the gray colored layer observed in Fig. 2b). Diffraction hyperbolas, which after the migration process almost completely collapse into the points labeled with H (Fig. 4a, from 0.2 to 1 m depth), may represent thick roots or small stones.

Figure 4b shows a zoom of the electrical resistivity section obtained from inversion of ERT measurements using $N=1$. The shallow levels are characterized by resistivities < 40 Ωm (bluish colors from 0 to 0.5 m in Fig. 4b), which likely represents soil partially wetted by the irrigation event that started when geophysical acquisition took place. However, ERT results observed approximately below 0.5 m should represent the electrical resistivity structure of a soil which has not been watered for more than 2 months. The more remarkable feature of this section is the spatial correlation between the top of the sandy loam unit (labelled SL in Fig. 4b) and the top of the domain of resistivities > 150 Ωm (red tones in Fig. 4b). This correlation suggests that the sandy loam horizon is characterized by resistivities > 150 Ωm under dry conditions.

Temporal variability in the electrical resistivity structure

To estimate the spatiotemporal distribution of soil moisture during irrigation, we analyzed the evolution over time of the electrical resistivity structure. Figures 5 and 6 show the preferred electrical resistivity sections obtained for all ERT measurement of January 2019 using $N=4$ and $N=1$, respectively. To put ERT results in the context of the irrigation cycle, Fig. 5 also displays the amount of VWC registered by the permanent TDR sensor located in the next vine row below a dripper. As a reference, we indicate the location of vines and drippers on top of each resistivity section. On the whole, ERT results suggest a layered structure which is consistent with soil units observed in the ~ 2 m-depth soil pit and on the GPR section. In fact, all resistivity models show an electrical resistivity structure roughly characterized by three major domains from top to bottom (see Figs. 5 and 6): a shallow domain from 0 to 0.5 m depth with resistivities < 50 Ωm (bluish color, labelled C1), a middle domain from 0.5 to 2 m depth in a range of 20–150 Ωm ("middle domain" in Fig. 5b), and a deep domain below 2 m depth with resistivities > 150 Ωm (reddish colors, "deep domain" in Fig. 5b).

Largest temporal variations in resistivity are observed from 0 to 0.5 m depth (labelled C1 in Figs. 5 and 6), a domain which partially coincides with the shallow soil units (L and SiL in Figs. 3b and 4). The resistivity of layer C1 decreases in those days following irrigation events (< 30 Ωm in January 10 and 16, blue tones in Figs. 5b, e and 6a, d), and increases during the driest days (> 50 Ωm in January 8 and 14, green tones in Figs. 5a, d and 6c). The increment of resistivity with time from irrigation events suggest that resistivity changes in C1 are controlled by irrigation water. Below layer C1, a group of bodies with resistivity > 100 Ωm is observed mostly from 0.5 to 1 m depth (features labelled R1 in Figs. 5 and 6). We interpret that R1 represent relatively drier zones due to root water uptake activity, because the average density of fine roots observed in the soil pit increases between 0.5 and 1 m depth (see right panel of Fig. 4b). The temporal variability of resistivity at R1 follows the opposite trend observed in C1. While the resistivity of R1 increases in days following irrigation (more segments with > 100 Ωm are observed in Figs. 5c, e and 6b, d), it tends to decrease during the driest days (predominantly between 50 and 70 Ωm, see greenish colors in Figs. 5a, d and 6c). We suggest that bulk resistivity at R1 is also controlled by soil moisture. In such a case, a relative increase of soil water content and its associated relative decrease in resistivity take place at late stages of each irrigation cycle, when the infiltrated irrigation water reaches the root zone. We test the feasibility of this hypothesis in the numerical simulations which are discussed later in "Spatiotemporal evolution of soil moisture".

Although all ERT models show a predominantly layered resistivity structure, significant variations of resistivity along the profile direction are observed at some depths. The largest lateral contrast in resistivity is observed below 1 m depth between $X=2$ and $X=6$ m (circular-shaped bluish zone labelled C2 in Fig. 5). We tested the sensitivity of the data to the presence of C2, by replacing the zone roughly occupied by C2 with a rectangular body with the average background resistivity at those depths (100 Ωm). The responses of these models do not reproduce well the data in the southern segment of the sections (approximately 40% of the data, see Fig. 12), obtaining a datafit which is significantly worse than the datafit obtained with the preferred models (compare Figs. 10 with 12 in the "Appendix"). From these tests we interpret that C2 is well supported by the data and required to explain the observations. The origin of C2 is not clear, but we suggest that can be related to the lens of sandy clay loam observed in the soil pit at 1.5 m depth from $X=4$ to $X=5$ m.

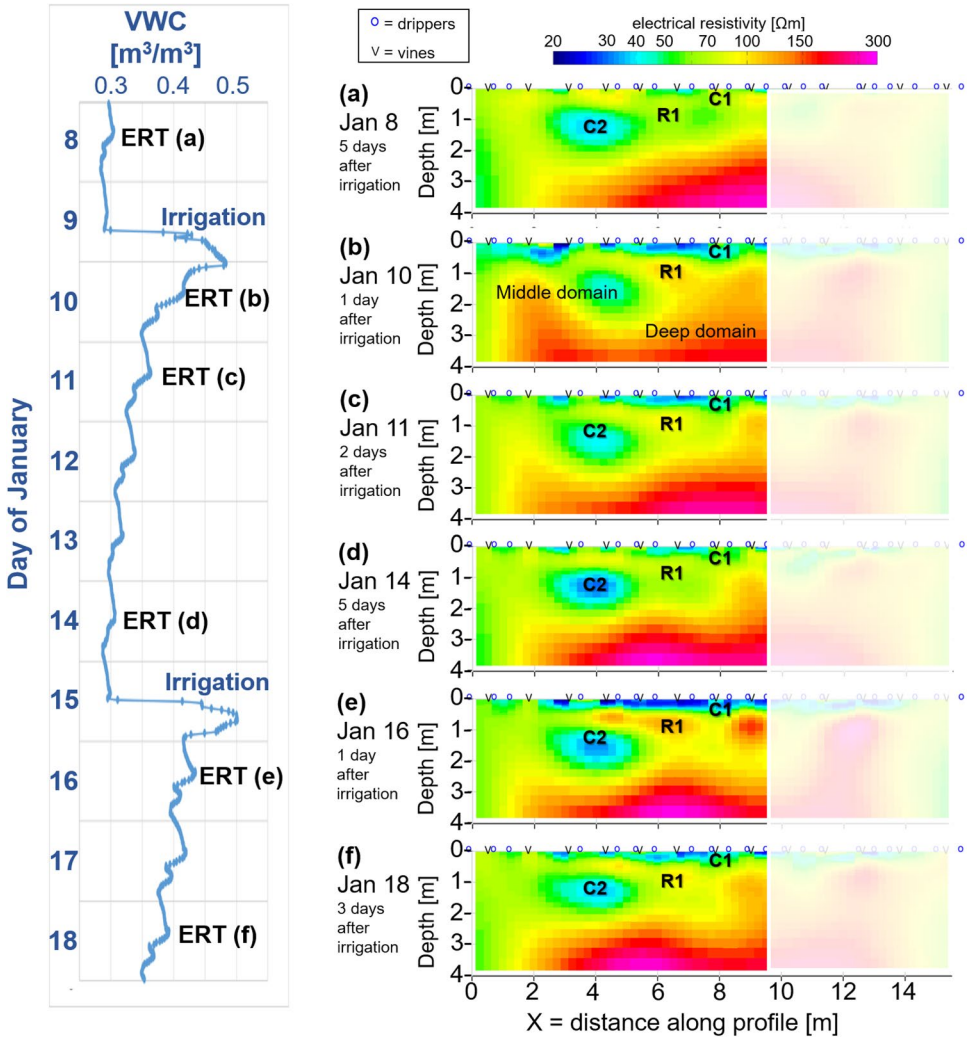

Fig. 5 Electrical resistivity tomography results ($N=4$). Left panel shows temporal variations of soil water content measured by TDR sensor installed in the vine row next to the studied row (see location in Fig. 1). The time when ERT measurements and irrigation took place are indicated. Right panel shows sections with preferred models of electrical resistivity obtained for each day using $N=4$. The pale box masks the segment of the sections with less reliable results. "V" and "O" on top of resistivity sections indicate position of grapevines and drippers, respectively. C1 indicates the layer from 0 to 0.5 m depth, which exhibits resistivities < 50 Ωm over all days. C2 is a circular-shaped zone with resistivities < 40 Ωm, which partially coincides with a lens of sandy clay loam observed in the soil pit. R1 refer to bodies with resistivity > 100 Ωm which are observed mostly from 0.5 to 1 m depth. See details in "Temporal variability in the electrical resistivity structure"

Discussion

Reliability of ERT monitoring results

The robustness of electrical resistivity models relies on multiple factors, but primarily on how well model responses fit measured ERT data, which in turns depend on the quality of ERT measurements. Both measuring errors and data misfit are comparable and quite small: while the analyzed data have measuring errors (repeatability) < 2% (see "ERT"), the misfit between model responses and observations for all ERT surveys mostly do not exceed 5% (see Tables 4 and 5). Although inversion of ERT data is characterized by non-unique solutions, all electrical resistivity models converge to a common electrical resistivity structure roughly characterized by three major and distinctive domains in terms of electrical resistivity range (see Figs. 5 and 6). The time-lapse exercise that implies geo-electrical measurements during different days within the irrigation cycle provides a mechanism to test the robustness of the applied geophysical methodology. Resistivity models derived from observations at different days show a first-order similarity between them, suggesting that the overall resistivity structure is well resolved and consistent.

Major lateral resistivity contrasts are observed at 0–2 m depth, a zone where changing physical conditions due to irrigation water are expected to alter the resistivity structure. However, shallow levels (< 1 m) of the resistivity model are also more prone to exhibit artefacts caused by errors in measurements of temperature and electrodes spacing. Therefore, the presence of resistivity artefacts must be addressed before interpreting lateral contrasts of resistivity at shallow levels as evidence of soil regions with poor irrigation uniformity. Although we corrected the effect of temperature on resistivity by calculating the resistivity value at 25 °C, some bias can be introduced in cells of the models located from 0 to 0.4 m depth due to the uncertainty of measured soil temperature. Yet, such errors are small for reasonable uncertainties in the measurement of temperature (e.g. a bias of 10% in temperature will not exceed an error of 5% in resistivity, see Brunet et al. 2010). Errors in the

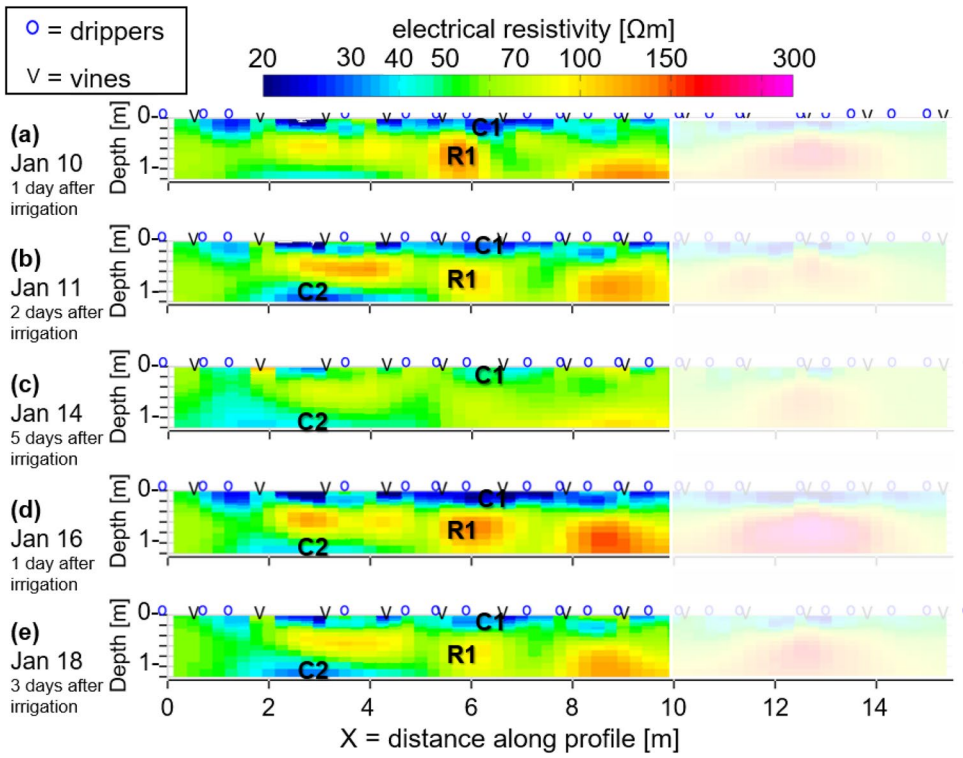

Fig. 6 Electrical Resistivity Tomography results ($N=1$). Sections with preferred models of electrical resistivity obtained for each day using $N=1$. Note that measurements with $N=1$ were not available for January 8. The pale box masks the segment of the sections with less reliable results. "V" and "O" on top of resistivity sections indicate position of grapevines and drippers, respectively. C1, C2 and R1 refer to resistivity features described in caption of Fig. 5 and "Temporal variability in the electrical resistivity structure"

estimation of electrode spacing can introduce bias on resistance measurements (Zhou and Dahlin 2003; Oldenborger et al. 2005). In our study, electrodes where installed every 0.5 m using a measuring tape as reference. We estimate that our error in each electrode's position does not exceed 2 cm, which implies an error of 8% in the estimation of dipoles length. For dipole–dipole arrays and a simple resistivity structure (e.g. a homogenous half-space or a two-layered model), Zhou and Dahlin (2003) show that errors of 10% in electrodes' spacing can produce error up to 20% in the measured resistance at shallow quadripoles located below mislocated electrodes. Consequently, we cannot exclude that some lateral variations in resistivity observed at C1 could be attributed to artefacts caused by some of the aforementioned factors. Therefore, it is difficult to draw conclusions about irrigation uniformity from 0 to 0.5 m depth. Nevertheless, lateral resistivity contrasts observed below 0.5 m are likely robust (e.g. around R1 bodies and C2, Figs. 5 and 6), especially considering their size (≥ 2 m length along the profile) and their distance from electrodes. These deeper resistivity contrasts suggest that the amount of infiltrated water is not uniformly distributed, at least, below 0.5 m depth.

Relationship between electrical resistivity and soil moisture

Observed resistivity changes can be attributed to changes in water content and/or soil properties (e.g. salinity) as a consequence of irrigation. We suggest that changes in soil moisture are the most likely candidate to explain variations in resistivity, mainly based on two reasons. First, the resistivity of the shallow layer (C1) decreases following irrigation events. Second, a resistivity of 5.9 Ωm was measured in the water used for irrigation, a value that is significantly lower than the average background resistivity observed in ERT sections of Figs. 4b, 5 and 6. If soil salinity were the most important factor controlling bulk soil resistivity in this area, we would expect to see an increase of resistivity following irrigation events in C1, as irrigation water may contribute to move away salts, and salts are usually characterized by very low resistivities. However, resistivity in C1 increases with days from the irrigation events (see "Temporal variability in the electrical resistivity structure" and Fig. 5 and 6).

To estimate quantitatively the spatiotemporal evolution of the soil moisture from ERT results, we analyzed the relationship between electrical resistivity and VWC values measured in situ (Fig. 7). In Fig. 7, triangles compare the average VWC values measured with FDR at each soil layer in the soil pit, with the average value of resistivity from model's cells at the same position obtained from resistivity model of ERT collected in September 23. Circles compare the average VWC values registered by fixed TDR sensor during each ERT measurement in January, and the average value of shallow cells from the corresponding ERT resistivity model. As the fixed TDR sensor is installed

below a dripper at 0.1 m depth, the corresponding resistivity value was calculated from all of those cells which were located from 0 to 0.3 m depth below drippers. As it is usually expected, electrical conductivity (reciprocal of resistivity) exhibits a direct proportionality with VWC. For sake of simplicity, a linear relation was fitted to the observed relationship, resulting in a large correlation coefficient ($R^2 = 0.93$).

A number of linear, polynomic, power-law, exponential and even more complex mathematical models have been proposed to relate soil moisture and electrical resistivity (see e.g. Michot et al. 2003; Brunet et al. 2010; Calamita et al. 2012; Brillante et al. 2014). Although we acknowledge that the available in situ VWC measurements are scarce, the linear relation shown in Fig. 7 fits reasonably well the relationship observed between both parameters. This simple relation suggests that the resistivity of the interstitial fluids is the main factor controlling the bulk resistivity of the soil. This interpretation would be also supported by the significant contrast observed between the resistivity measured in the irrigation water (5.9 Ωm) and the average resistivity of the soil imaged by the ERT survey acquired in September (> 100 Ωm, Fig. 4b). However, the electrical resistivity of a volume of soil depends on a number of factors, being usually the most important the electrical resistivity and amount of interstitial fluids, but also the resistivity of mineral grains, the interconnectivity between voids containing fluids, and temperature, among others (e.g. Friedman 2005). We predict that our simple linear relationship may not describe well the relationship between resistivity and soil moisture in clay-rich soils or in areas where irrigation water and soils show low resistivity contrasts. In such environments, the bulk soil resistivity can be highly sensitive to the resistivity and amount of mineral grains (see e.g. Waxman and Smits 1968), making difficult to use electrical resistivity as a proxy for the soil moisture distribution. This fact points out that the relationship between electrical resistivity and soil moisture must be estimated locally at each field, as it has been widely discussed in the literature (Boaga et al. 2013; Moreno et al. 2015; Cassiani et al. 2016; Hardie et al. 2018). In particular, the resistivity of the irrigation water must be known in order to assess the applicability of the ERT as monitoring tool to estimate soil moisture distribution.

Spatiotemporal evolution of soil moisture

Figure 8 shows the temporal evolution of soil moisture derived from resistivity models of ERT surveys using $N = 4$. Estimated VWC values (θ_{ERT}) were obtained from resistivity using the mathematical relationship shown in Fig. 7. Figure 8a displays the soil moisture as the absolute

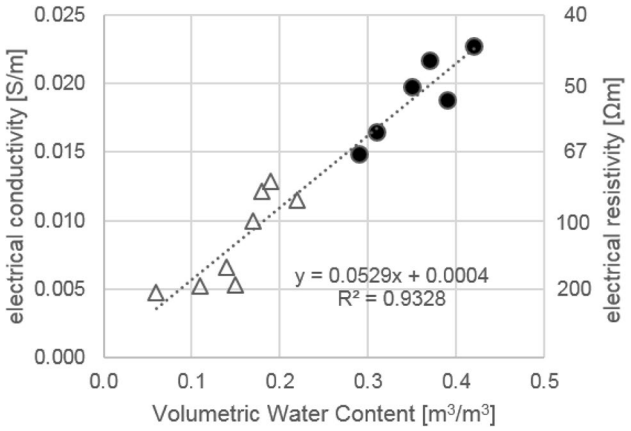

Fig. 7 Relationship between volumetric water content (VWC) and electrical conductivity (derived from electrical resistivity models) obtained at equivalent positions (see detailed description in "Relationship between electrical resistivity and soil moisture"). White triangles compare VWC measured in the soil pit with FDR and resistivity values obtained from ERT survey conducted in September 2019. Black circles compare VWC measured by TDR sensor in next grape row and resistivity values obtained from ERT measurements made in January. The dotted line is a linear model that fits the data

value of θ_{ERT} derived from resistivity model of January 8. To analyze the relative variation of soil moisture over days, Fig. 8b–f display the difference of VWC between each day and the VWC of January 8, that is: $\Delta\theta_{ERT} = \theta_{ERT}(\text{day}) - \theta_{ERT}$ (January 8). The aim of analyzing differences of estimated VWC is to detect significant relative changes in soil moisture during the irrigation cycle, regardless of the absolute value of VWC at any reference day, which is difficult to estimate accurately with indirect methods. Figure 8 shows a clear contrast in the soil moisture content variations ($\Delta\theta_{ERT}$) between layers C1 and R1 over both irrigation cycles. C1 exhibits a relative surplus in soil moisture (blue tones in Fig. 8b–f), likely indicating that some water remains stored at this layer. Conversely, R1 is characterized by a moisture deficit relative to January 8 (red tones in Fig. 8b–f), condition that we interpret as evidence of lower VWC maintained by the continuous root water uptake. A structure of relatively high soil moisture seems to connect C1 and C2 during January 14, 16 and 18 (see arrows in Fig. 8d–f). We suggest that this structure represents a soil heterogeneity with high hydraulic conductivity, which could channel irrigation water into C2 and therefore explains the anomalously high θ_{ERT} at C2 during all days (e.g. $\theta_{ERT} > 0.4$ in Fig. 8a). We speculate that deeper zones that exhibit relatively higher soil moisture can also represent some zones where irrigation water may accumulate as in C2 (see bluish colors below 2 m depth between $X = 4$ and $X = 10$ m in Fig. 8b–f).

The spatiotemporal evolution of VWC derived from ERT monitoring (Fig. 8) suggests a nonuniform distribution of irrigation water, especially below 0.5 m depth. However,

we do not have independent information to check how well the ERT models estimate VWC aside at the soil pit or closer to the TDR sensor. Moreover, this estimate does not provide information about the overall amount of water that is leaking below the root zones in the studied vine row. To address these questions, we performed numerical modeling to simulate the spatiotemporal distribution of soil moisture under conditions similar to the studied vine row (see model details in "Numerical model of spatiotemporal distribution of soil moisture"). Figure 9 compares the distribution of soil moisture with depth obtained from our numerical modeling analysis and from electrical resistivity sections. Soil moisture is displayed as the difference ($\Delta\theta$) between the VWC obtained at each day with respect to the VWC obtained at the fifth (last) day of the irrigation cycle. The soil moisture estimated from electrical resistivity sections measured with $N=4$ was taken as the VWC stored in the soil for different days and depths. Figure 9a and b show the results of the numerical models A and B (respectively) evaluated at the equivalent times (days) from irrigation events at which ERT surveys took place. Each line in Fig. 9c represents the variation of θ_{ERT} with depth at ERT acquisition dates, obtained after averaging all VWC values derived from resistivity model' cells located at the same depth.

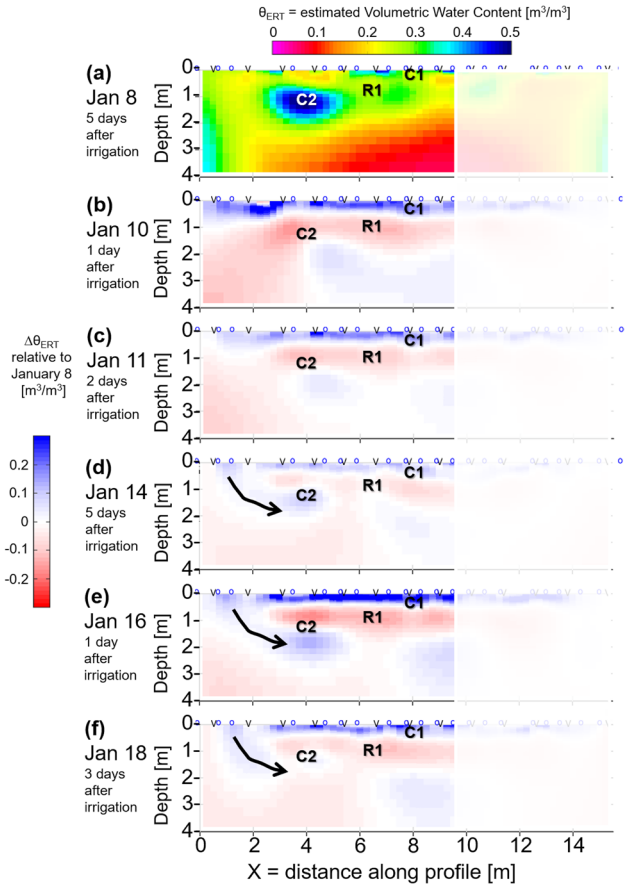

Fig. 8 Distribution of soil moisture interpreted from ERT monitoring in January 2019. **a** Estimated volumetric water content from resistivity sections (θ_{ERT}) obtained for January 8th. **b–f** Difference of estimated volumetric water content between each day and January 8th, that is: $\Delta\theta_{ERT}=\theta_{ERT}$ (day) $-\theta_{ERT}$ (January 8th). C1, C2 and R1 refer to resistivity features described in caption of Fig. 5 and "Relationship between electrical resistivity and soil moisture". The pale box masks the segment of the sections with less reliable results

The variability of $\Delta\theta$ with depth and time derived from numerical models and ERT estimates show a similar shape, but differences in the absolute value of $\Delta\theta$. All estimates exhibit the same general pattern (see Fig. 9): from 0 to ~ 0.5 m depth $\Delta\theta$ is larger in days closer to the irrigation event (e.g. blue lines, which indicate January 10 and/or 1 day after irrigation), at ~ 0.5 m depth $\Delta\theta$ is closer to zero for all days, and from ~ 0.5 to ~ 1.5 m depth $\Delta\theta$ is larger at later days of the irrigation cycle (e.g. red lines, which indicate January 14 = 4 days after irrigation). Overall, this pattern suggests that soil moisture decreases with time from the irrigation event from 0 to ~ 0.5 m depth. However, from ~ 0.5 to ~ 1.5 m depth the opposite trend is observed, suggesting that soil moisture tend to increase with time from the irrigation event. In the numerical model, this trend is strongly controlled by the sink function that simulates the effect of root water uptake (see "Numerical model of spatiotemporal distribution of soil moisture" and Eq. 2), which was prescribed to the depth range where roots are concentrated (gray area in Fig. 9). While $\Delta\theta$ approaches to zero almost immediately below the gray area (= root zone) in the numerical simulations (Fig. 9a, b), $\Delta\theta$ converges to zero for depths below 2 m in the soil moisture estimate derived from ERT (Fig. 9c). We interpret that non-zero $\Delta\theta$ values obtained from ERT at 1.5–2 m depth indicates that some soil moisture variability, triggered by irrigation events, is lost below the root zone, suggesting deep percolation of irrigation water.

The relative variability of soil moisture with depth and time derived from ERT surveys is consistent with results obtained from our numerical modeling of Richards equation (Fig. 9). This correlation proofs that relative variations of VWC estimated from ERT are physically meaningful, that is, that they roughly reproduce the spatiotemporal distribution expected for water moving in a partially saturated porous medium. In particular, this correlation validates ERT results suggesting that some irrigation water percolates below the root zone. For detecting deep percolation, therefore, the application of the ERT seems to be a good cost-effective mean. However, the absolute values of soil moisture derived from ERT do not necessarily fit our numerical modeling results (only $\Delta\theta$ absolute values of blue, green and red lines partially coincides in Fig. 9b, c). There are several factors that may influence the accuracy of ERT estimates of soil moisture, including ERT data quality, resistivity contrast between irrigation water and soil components, fractionation of irrigation water components, and soil properties (see e.g.

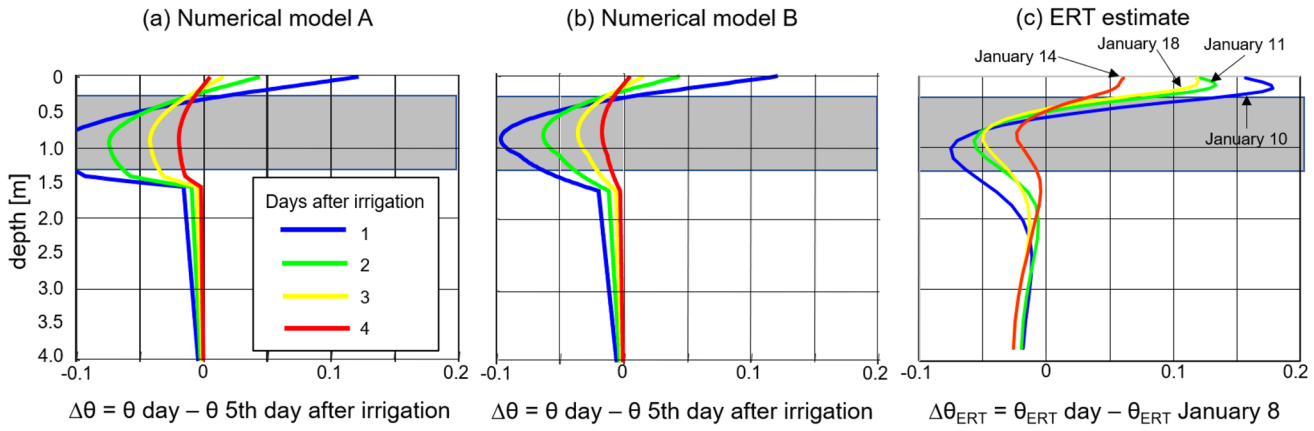

Fig. 9 Comparison of spatiotemporal variation of soil moisture obtained from numerical models **a** A and **b** B, and **c** estimate derived from resistivity models obtained from ERT measured using $N=4$. The gray area indicates the depth where the sink function extracts water in our numerical model, which is the depth with the maximum concentration of thin roots observed at the soil pit

Boaga et al. 2013; Moreno et al. 2015; Hardie et al. 2018). For this reason, it is important to remark that ERT can be used as a tool for detecting significant relative changes in soil moisture, but it does not provide accurate enough estimates of VWC's absolute values in order to quantify the amount of water loss.

Implications for irrigation management

When there are significant differences between average soil resistivity and the resistivity of irrigation water (see previous discussion), our results suggest that ERT monitoring can detect relative changes in soil moisture distribution during irrigation. If such condition is verified, estimates of soil moisture derived from ERT studies can provide valuable information to assess the efficiency of irrigation systems. In practice, irrigation plans are usually decided using, at best, information collected at point measurements of evapotranspiration and soil moisture. However, practical problems can arise by assuming homogenous characteristics in soil hydraulic properties. For instance, in the studied vineyard, irrigation is managed based on information provided by a nearby automatic weather station. With this information, reference evapotranspiration (ETo) is calculated and irrigation system is set up to supply a fraction of cumulative ETo which is slightly above the crop coefficient ($K_c=0.65$). During the ERT monitoring experiment, the estimated crop evapotranspiration (ET_c) reached 22.9 and 19.8 mm before the irrigation events occurring on January 9 and January 15, respectively. Therefore, in order to ensure crop water demands, the amount of water applied in these irrigation events was equivalent to 27 mm (1 mm = 1 kg/m^2), a value which exceeds the maximum ET_c. However, the applied water largely exceeded the cumulative actual evapotranspiration measured locally at the studied vineyard by the EC tower before these irrigation events (13.9 and 13.1 mm). We interpret that this excess of applied water may flew through soil domains with relatively large hydraulic conductivity, explaining the deep percolation suggested by ERT results (e.g. the temporal evolution of resistivity feature C2 shown in Fig. 8).

The previous analysis highlights that monitoring meter-scale changes in soil electrical resistivity during an irrigation cycle can provide useful information for assessing the local efficiency of an irrigation system. To apply ERT for evaluating the performance of irrigation at the orchard-scale, we propose a three-stage acquisition strategy. In the first stage, to conduct massive GPR measurements in order to identify domains with distinctive soil stratigraphy within the studied orchard. The acquisition of GPR under flat terrain condition is relatively fast, and consequently can cover a plot in a couple of days. In the second stage, to conduct ERT monitoring in selected rows of soil domains interpreted from GPR. The aim of the second stage is to infer the spatiotemporal distribution of soil moisture at some representative zones, in order to estimate irrigation uniformity and to detect possible deep percolation. ERT monitoring at each zone must take place at least over one complete irrigation cycle, ideally in a daily basis, to maximize the number of observations that are necessary for evaluating the relationship between resistivity variations and expected changes in soil moisture. We recommend to follow the parameters described in this work for conducting the ERT monitoring experiments. Finally, ERT and GPR results can be verified with soil moisture measurements and soil stratigraphy characterization made at some soil pits. The joint interpretation of GPR, ERT monitoring and soil pit characterization can be used, therefore, to estimate the spatiotemporal distribution of applied water during irrigation and to identify areas with distinctive soil hydraulic properties within an orchard.

Conclusions

We evaluated the reliability of ERT to constrain irrigation uniformity and deep percolation at the scale of meters. Our findings show that relative changes of soil moisture with depth and time estimated from ERT images are consistent with the spatiotemporal evolution of VWC expected for a partially saturated porous medium under irrigation. This correlation suggests that ERT provides physically meaningful results that can be used to monitor the relative variability of soil moisture over time, if two conditions are verified in the field. First, ERT measurements must take place at different stages of a couple of irrigation cycles, to identify spatiotemporal variations in soil electrical resistivity which are coherent with expected relative changes in VWC triggered by the infiltration of applied water. Second, the electrical resistivity of irrigation water should be significantly lower than the average soil electrical resistivity. In the studied vineyard, the electrical resistivity of irrigation water is 20 times lower than the average bulk resistivity of the soil under dry conditions.

Largest temporal variations of electrical resistivity were observed at depths < 0.5 m, indicating that soil moisture in the studied vine row mostly changes within the root depth (1 m depth). However, electrical resistivity variations were also observed from 1 to 2 m depth, suggesting that some water percolated below the root zone. This interpretation is consistent with the fact that the amount of water applied during the experiment largely exceeded the actual evapotranspiration measured at the vineyard. ERT images exhibit lateral variations in electrical resistivity that indicate the presence of preferential pathways in the distribution of moisture with depth. Altogether, our study indicates that time-lapse ERT provides useful information to constrain irrigation uniformity and to detect deep percolation at orchard scale during an irrigation season. ERT monitoring can be used, therefore, to identify zones with distinctive soil hydraulic properties within an orchard. ERT results, in combination with co-located GPR profiles and calibration at some soil pits, can be used to interpret the nature of soil properties changes and to assess their role in irrigation efficiency. With this information, irrigation plans can be specifically tailored to local hydraulic conditions in order to meet, with more precision, crop water demand.

Acknowledgements This work was funded by FONDECYT Grant 1170429 and partially supported by FONDECYT Grant 1181392. We gratefully acknowledge Pedro Ruiz-Tagle (vineyard landowner) and Pedro Mesina (vineyard manager) for allowing us to conduct this study and their logistical support. We thank Fernanda Gallegos, Sergio Gutiérrez, Matías Lillo, Catalina Lizarde, María Cecilia Muñoz, Francisco Suárez and Damián Tosoni for helping during geophysical measurements. We wish to thank the two anonymous reviewers and the editor for their comments, which significantly contributed to improve the original version of this paper. We thank Zond Software© for the demo version of Zondres2d available at http://zond-geo.com/english/. Jaime Araya Vargas was financially supported by FONDECYT Postdoctoral Grant 3180182. Data can be requested by contacting Jaime Araya Vargas (jaarayav@ing.puc.cl).

Funding Fondo Nacional de Ciencia y Tecnología (FONDECYT) Grant 1170429.

Availability of data and materials Requests for data and materials should be addressed to Jaime Araya Vargas.

Compliance with ethical standards

Conflict of interest On behalf of all authors, the corresponding author states that there is no conflict of interest

Appendix: ERT data fit

Tables 4 and 5 show the misfit between observations and preferred inversion models' responses for all ERT surveys made with $N=4$ and $N=1$, respectively. Initial RMS error is the average misfit between observations and the response of the starting model (a 70 Ωm homogenous half space). The data misfit range indicates the differences between measured data and model responses observed overall quadripoles, expressed as percentage of the measured data value (Figs. 10, 11, 12).

Table 4 Misfit for preferred models of ERT surveys made with $N=4$

ERT survey	Initial RMS error	Final RMS error	Data misfit range (%)	Number of Iterations	RMS error model shown in Fig. 12
January 8	14.8	0.92	−3.9 to 3.3	2	7.1
January 10	16.4	1.37	−4.2 to 5.3	2	4.5
January 11	15.6	1.07	−4.5 to 4	2	5.3
January 14	15.3	0.96	−2.6 to 1.9	2	6.6
January 16	16.5	1.29	−4.7 to 5.1	2	4.6
January 18	15.7	1.18	−4.2 to 5.6	2	5.7

Table 5 Misfit for preferred models of ERT surveys made with $N=1$

ERT survey	Initial RMS error	Final RMS error	Data misfit range (%)	Number of iterations
January 10	9.3	1.19	−5.8 to 5.4	3
January 11	8.2	1.17	−1.5 to 1.4	2
January 14	5.9	0.91	−4.3 to 3.9	2
January 16	10.2	1.18	−2.1 to 2.0	2
January 18	7.0	0.98	−2.2 to 1.6	2

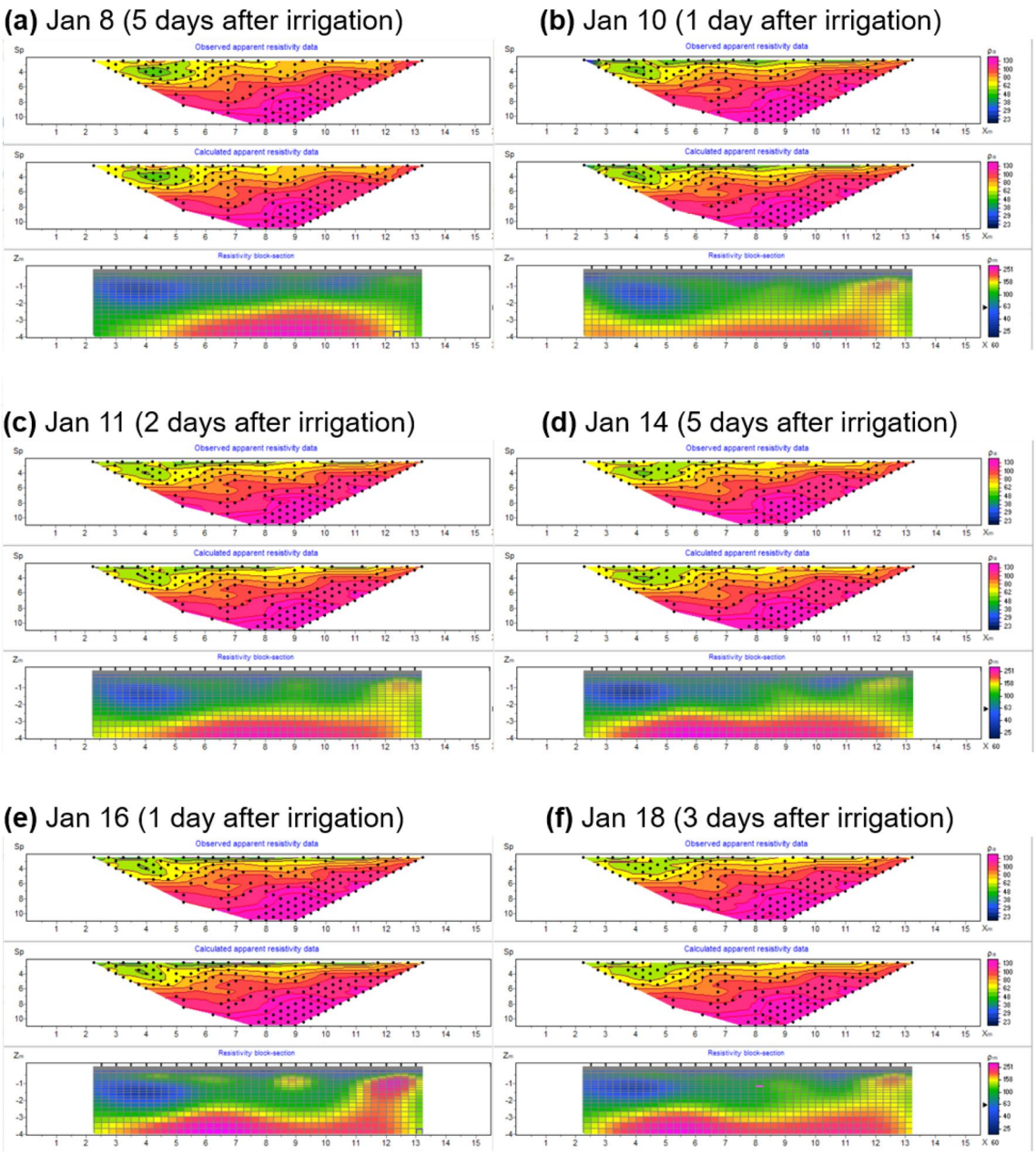

Fig. 10 Comparison between observations and preferred model responses for ERT surveys made with $N=4$. For each day, upper panel shows the pseudosection calculated from observed data, middle panel shows the pseudosection calculated from the inversion resistivity model, and lower panel shows the inversion resistivity model. Black dots in pseudosections indicate the estimated location of apparent resistivity points measured with each quadripole

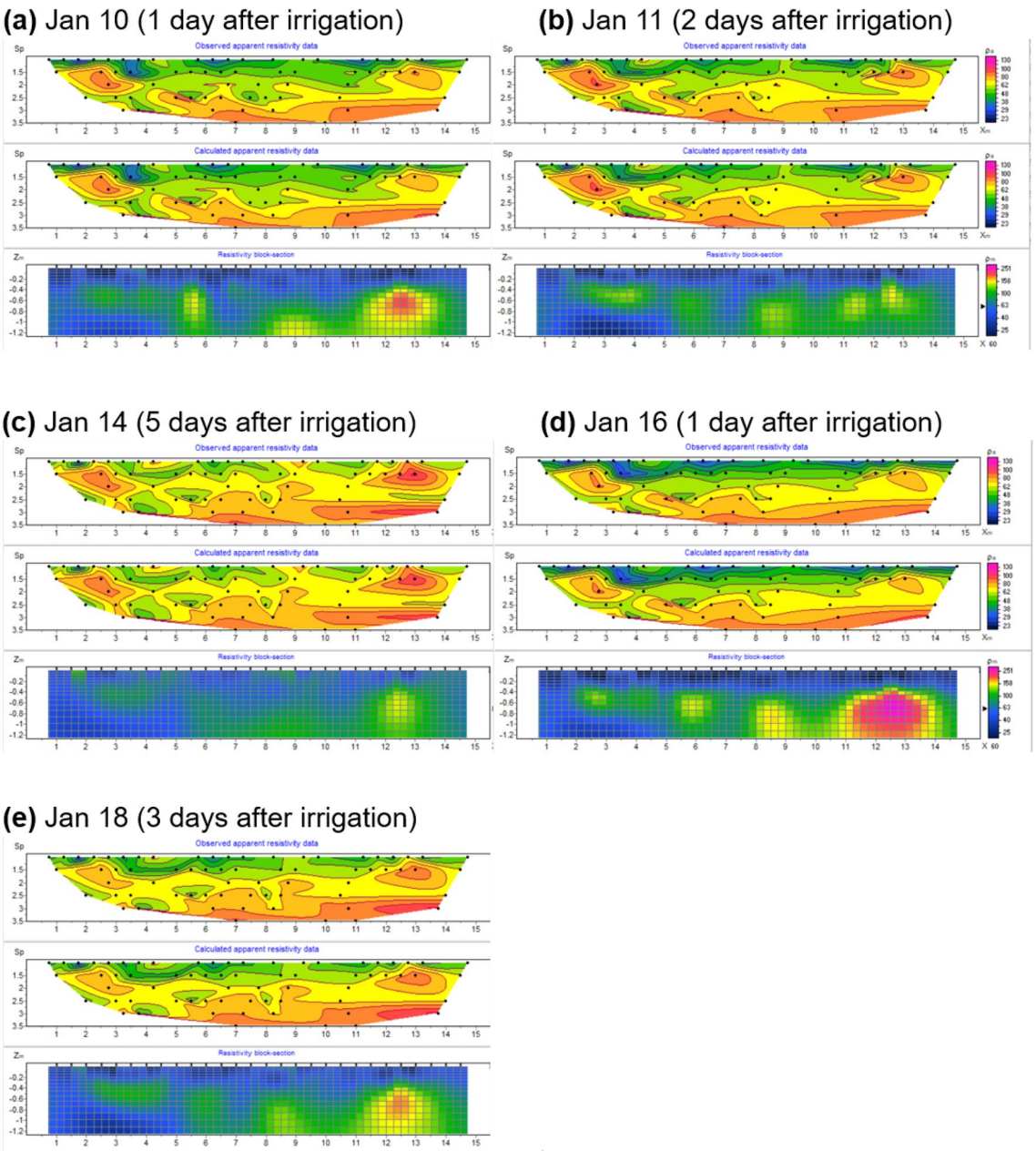

Fig. 11 Comparison between observations and preferred model responses for ERT surveys made with $N=1$. For each day, upper panel shows the pseudosection calculated from observed data, middle panel shows the pseudosection calculated from the inversion resistivity model, and lower panel shows the inversion resistivity model. Black dots in pseudosections indicate the estimated location of apparent resistivity points measured with each quadripole

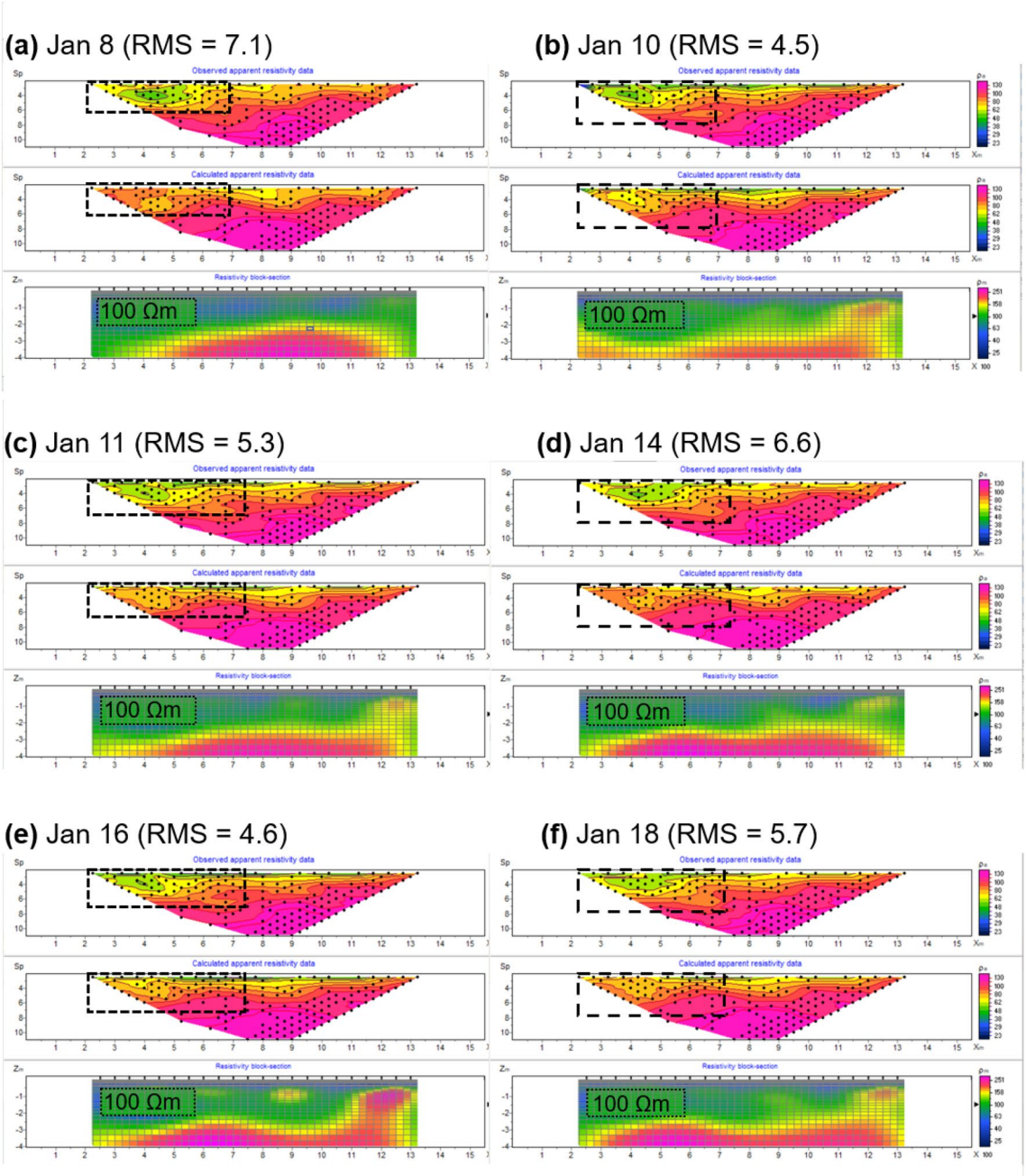

Fig. 12 Sensitivity test of resistivity feature C2 for ERT surveys made with $N=4$. Comparison between observations and responses of a modified version of the preferred model, where a 100 Ωm rectangle replaces the area roughly occupied by C2 in the preferred model. For each day, upper panel shows the pseudosection calculated from observed data, middle panel shows the pseudosection calculated from the inversion resistivity model, and lower panel shows the inversion resistivity model. Dashed-line polygons in pseudsections panels outline the areas where the datafit is worse than in the preferred model responses. Dotted-line polygons in model panels outline the 100 Ωm rectangle that was added to the preferred model. Global RMS error for each model is indicated

References

Alamry AS, van der Meijde M, Noomen M, Addink EA, van Benthem R, de Jong SM (2017) Spatial and temporal monitoring of soil moisture using surface electrical resistivity tomography in Mediterranean soils. CATENA 157:388–396

Allred B, Daniels JJ, Ehsani MR (2008) Handbook of agricultural geophysics. CRC Press, Boca Raton

André F, van Leeuwen C, Saussez S, Van Durmen R, Bogaert P, Moghadas D, de Rességuier L, Delvaux B, Vereecken H, Lambot S (2012) High-resolution imaging of a vineyard in south of France using ground-penetrating radar, electromagnetic induction and electrical resistivity tomography. J Appl Geophys 78:113–122

Boaga J, Rossi M, Cassiani G (2013) Monitoring soil-plant interactions in an apple orchard using 3-D electrical resistivity tomography. Procedia Environ Sci 19:394–402. https://doi.org/10.1016/j.proenv.2013.06.045

Bouyoucos GJ (1962) Hydrometer method improved for making particle size analysis of soils. Agron J 54:464–465

Brillante L, Bois B, Mathieu O, Bichet V, Michot D, Lévêque J (2014) Monitoring soil volume wetness in heterogeneous soils by electrical resistivity. A field-based pedotransfer function. J Hydrol 516:56–66

Brower C, Prins K, Heilbloem M (1989) Irrigation water management: irrigation scheduling, training manual no. 4. FAO, Rome

Brunet P, Clément R, Bouvier C (2010) Monitoring soil water content and deficit using Electrical Resistivity Tomography (ERT)–a case study in the Cevennes area, France. J Hydrol 380(1–2):146–153

Calamita G, Brocca L, Perrone A, Piscitelli S, Lapenna V, Melone F, Moramarco T (2012) Electrical resistivity and TDR methods for soil moisture estimation in central Italy test-sites. J Hydrol 454:101–112

Cassiani G, Boaga J, Vanella D, Perri MT, Consoli S (2015) Monitoring and modelling of soil–plant interactions: the joint use of ERT, sap flow and eddy covariance data to characterize the volume of an orange tree root zone. Hydrol Earth Syst Sci 19(5):2213–2225. https://doi.org/10.5194/hess-19-2213-2015

Cassiani G, Boaga J, Rossi M, Putti M, Fadda G, Majone B, Bellin A (2016) Soil–plant interaction monitoring: small scale example of an apple orchard in Trentino, North-eastern Italy. Sci Total Environ 543:851–861. https://doi.org/10.1016/j.scitotenv.2015.03.113

Constable SC, Parker RL, Constable CG (1987) Occam's inversion: a practical algorithm for generating smooth models from electromagnetic sounding data. Geophysics 52(3):289–300

Cunningham RL, Matelski RP (1968) Bulk density measurements on certain soils high in coarse fragments. Soil Sci Soc Am Proc 32:109–111

Dai A (2013) Increasing drought under global warming in observations and models. Nat Clim Change 3(1):52–58. https://doi.org/10.1038/nclimate1633

DGA (2012). Estrategia Nacional de Recursos Hídricos 2012-2025. Ministerio de Obras Públicas. https://www.mop.cl/Documents/ENRH_2013_OK.pdf. Accessed Dec 2019

Evett SR, Parkin GW (2005) Advances in soil water content sensing: the continuing maturation of technology and theory. Vadose Zone J 4:986–991

Friedman SP (2005) Soil properties influencing apparent electrical conductivity: a review. Comput Electron Agric 46(1–3):45–70

Garré S, Javaux M, Vanderborght J, Pagès L, Vereecken H (2011) Three-dimensional electrical resistivity tomography to monitor root zone water dynamics. Vadose Zone J 10(1):412–424

Garreaud RD, Alvarez-Garreton C, Barichivich J, Boisier JP, Christie D, Galleguillos M, LeQuesne C, McPhee J, Zambrano-Bigiarini M (2017) The 2010–2015 megadrought in central Chile: impacts on regional hydroclimate and vegetation. Hydrol Earth Syst Sci 21(12):6307–6327. https://doi.org/10.5194/hess-21-6307-2017

Garreaud RD, Boisier JP, Rondanelli R, Montecinos A, Sepúlveda HH, Veloso-Aguila D (2019) The central Chile mega drought (2010–2018): a climate dynamics perspective. Int J Climatol. https://doi.org/10.1002/joc.6219

Greaves RJ, Lesmes DP, Lee JM, Toksöz MN (1996) Velocity variations and water content estimated from multi-offset, ground-penetrating radar. Geophysics 61(3):683–695

Hagrey SA, Müller C (2000) GPR study of pore water content and salinity in sand. Geophys Prospect 48:63–86. https://doi.org/10.1046/j.1365-2478.2000.00180.x

Hardie M, Ridges J, Swarts N, Close D (2018) Drip irrigation wetting patterns and nitrate distribution: Comparison between electrical resistivity (ERI), dye tracer, and 2D soil–water modelling approaches. Irrig Sci 2018(36):97–110

Hubbard S, Grote K, Rubin Y (2002) Mapping the volumetric soil water content of a California vineyard using high-frequency GPR ground wave data. Lead Edge 21(6):552–559. https://doi.org/10.1190/1.1490641

Huisman JA, Hubbard SS, Redman JD, Annan AP (2003) Measuring soil water content with ground penetrating radar. Vadose Zone J 2(4):476–491

Israelsen OW (1950) Irrigation principles and practices, vol 471. Wiley, New York

Keller GV, Frischknecht FC (1966) Electrical methods in geophysical prospecting. Pergamon Press, Oxford, p 517p

Kljun N, Rotach MW, Calanca P (2004) A simple parameterisation for flux footprint predictions. Bound Lay Meteorol 112:503–523

Kljun N, Calanca P, Rotach MW, Schmid HP (2015) A simple two-dimensional parameterisation for Flux Footprint Prediction (FFP). Geosci Model Dev 8:3695–3713. https://doi.org/10.5194/gmd-8-3695-2015

Klotzsche A, Jonard F, Looms MC, van der Kruk J, Huisman JA (2018) Measuring soil water content with ground penetrating radar: a decade of progress. Vadose Zone J 17(1):1–9

Kowalski AS, Anthoni PM, Vong RJ et al (1997) Deployment and evaluation of a system for ground-based measurement of cloud liquid water turbulent fluxes. J Atmos Ocean Tech 14:468–479. https://doi.org/10.1175/1520-0426(1997)014%3c0468:DAEOAS%3e2.0.CO;2

Lowrie W (2007) Fundamentals of geophysics. Cambridge University Press, Cambridge

Marchant M, Cecioni A, Figueroa S, González H, Giglio S, Hebbeln D, Kaiser J, Lamy F, Mohtadi M, Pineda V, Romero O (2007) Marine geology, oceanography and climate. In: Moreno T, Gibbons W (eds) The geology of Chile. Geological Society of London, London. https://doi.org/10.1144/GOCH.11

Mary B, Peruzzo L, Boaga J, Schmutz M, Wu Y, Hubbard SS, Cassiani G (2018) Small-scale characterization of vine plant root water uptake via 3-D electrical resistivity tomography and mise-à-la-masse method. Hydrol Earth Syst Sci 22:5427–5444. https://doi.org/10.5194/hess-22-5427-2018

Mary B, Vanella D, Consoli S, Cassiani G (2019) Assessing the extent of citrus trees root apparatus under deficit irrigation via multi-method geo-electrical imaging. Sci Rep 9:9913. https://doi.org/10.1038/s41598-019-46107-w

Meza FJ, Vicuña S, Jelinek M, Bustos E, Bonelli S (2014) Assessing water demands and coverage sensitivity to climate change in the urban and rural sectors in Central Chile. J Water Clim Change 5(2):192–203

Michot D, Benderitter Y, Dorigny A, Nicoullaud B, King D, Tabbagh A (2003) Spatial and temporal monitoring of soil water content with an irrigated corn crop cover using surface electrical resistivity tomography. Water Resour Res 39(5):1138. https://doi.org/10.1029/2002WR001581

Moreno Z, Arnon-Zur A, Furman A (2015) Hydro-geophysical monitoring of orchard root zone dynamics in semi-arid region. Irrig Sci 33(4):303–318. https://doi.org/10.1007/s00271-015-0467-3

Morlat R, Jacquet A (1993) The soil effects on the grapevine root system in several vineyards of the Loire valley (France). Vitis 32:35–42

Oldenborger GA, Routh PS, Knoll MD (2005) Sensitivity of electrical resistivity tomography data to electrode position errors. Geophys J Int 163(1):1–9

Reverter BR, Sánchez-Cañete EP, Resco V et al (2010) Analyzing the major drivers of NEE in a Mediterranean alpine shrubland. Biogeosciences 7:2601–2611. https://doi.org/10.5194/bg-7-2601-2010

Reynolds SG (1970) The gravimetric method of soil moisture determination, Part I. A study of equipment, and methodological problems. J Hydrol 11:258–273

Richards LA (1931) Capillary conduction of liquids through porous mediums. Physics 1:318–333

Robinson DA, Campbell CS, Hopmans JW, Hornbuckle BK, Jones SB, Knight R, Ogden F, Selker J, Wendroth O (2008) soil moisture measurement for ecological and hydrological watershed-scale observatories: a review. Vadose Zone J 7:358–389

Samouëlian A, Cousin I, Tabbagh A, Bruand A, Richard G (2005) Electrical resistivity survey in soil science: a review. Soil Tillage Res 83(2):173–193

Sandmeier, K.J. (2019) ReflexW Version 9. Program for processing of seismic, acoustic or electromagnetic reflection, refraction and transmission data. Software Manual, Karlsruhe, Germany

Schaap MG (2002) Rosetta: a computer program for estimating soil hydraulic parameters with hierarchical pedo-transfer functions (Version 1.2). http://cals.arizona.edu/research/rosetta/rosetta.html

USDA (US Department of Agriculture) (1977) National soil survey handbook, title 430-VI. Part 618.87 Texture Triangle and Particle-Size Limits of AASHTO. USDA and Unified Classification Systems, Washington DC

Valdés-Pineda R, Pizarro R, García-Chevesich P, Valdés JB, Olivares C, Vera M, Balocchi F, Pérez F, Vallejos C, Fuentes R, Abarza A, Helwig B (2014) Water governance in Chile: availability, management and climate change. J Hydrol 519(PC):2538–2567

Van Genuchten MT (1980) A closed-form equation for predicting the hydraulic conductivity of unsaturated soils 1. Soil Sci Soc Am J 44(5):892–898

Vanella D, Cassiani G, Busato L, Boaga J, Barbagallo S, Binley A, Consoli S (2018) Use of small scale electrical resistivity tomography to identify soil-root interactions during deficit irrigation. J Hydrol 556:310–324. https://doi.org/10.1016/j.jhydrol.2017.11.025

Waxman MH, Smits LJM (1968) Electrical conductivities in oil-bearing shaly sands. Soc Petrol Eng J 8(02):107–122

Webb EK, Pearman GI, Leuning R (1980) Correction of flux measurements for density effects due to heat and water vapour transfer. Q J R Meteorol Soc 106:85–100

Zhou B, Dahlin T (2003) Properties and effects of measurement errors on 2D resistivity imaging surveying. Near Surf Geophys 1(3):105–117

Zond Geophysical Software (2016). ZondRes2D. Program for two-dimensional interpretation of data obtained by resistivity and induced polarization methods (land, borehole and marine variants). Saint-Petersburg, 2010–2016